INTERNATIONAL JOURNAL FOR NUMERICAL METHODS IN ENGINEERING
Int. J. Numer. Meth. Engng (2007)
Published online in Wiley InterScience (www.interscience.wiley.com). DOI: 10.1002/nme.2228

Infinite boundary elements for electromagnetics

Edmund Chadwick*, †

School of Computing, Science and Engineering, University of Salford, Salford M5 4WT, U.K.

SUMMARY

Consider a two-dimensional plane wave transverse magnetic mode scattering from a perfectly electric conducting ground plane. Let the ground plane be of infinite extent and comprise two regions, a near field and a far field. In the far field, let the ground plane be flat and let us choose the co-ordinates (x, y) such that it lies on the axis $y=0$. Over the interior region, let the profile of the ground plane change such that it can lie partially above and also partially below the axis $y=0$. Finally, let us assume that the source of the excitation lies above the ground plane.

To model this general class of problems, a method of moments electric field integral equation formulation is proposed which uses infinite boundary elements to model the far field and boundary elements to model the near field. In the far field, the field variable is approximated by the highest order terms in the far-field asymptotic expansion. The integrals over the infinite boundary elements are infinite in extent and contain oscillatory terms and hence require special integration rules.

The formulation is tested for the specific problem of a semi-circular cylindrical protrusion of radius a lying above an infinite flat ground plane, such that $ka=1$ where k is the wave number. This problem is chosen because it has an analytic solution in the form of a Bessel function expansion; hence, the accuracy of the formulation can be tested. In particular, the radar cross section results for various angles of incidence of the plane wave source are calculated and compared with analytic results. Copyright © 2007 John Wiley & Sons, Ltd.

Received 28 June 2006; Revised 18 September 2007; Accepted 28 September 2007

KEY WORDS: infinite boundary elements; method of moments; ground planes; slots

1. INTRODUCTION

Small features embedded within larger structures, such as protrusions, fins, apertures, gaps, cracks, cavities and slots, can contribute significantly to the radar cross section (RCS). Because of the discrepancy in length scales, the dimensions of the embedded feature being an order of magnitude lower than the dimensions of the body, modelling their effect on the RCS can prove to be difficult.

*Correspondence to: Edmund Chadwick, School of Computing, Science and Engineering, University of Salford, Salford M5 4WT, U.K.
†E-mail: e.a.chadwick@salford.ac.uk

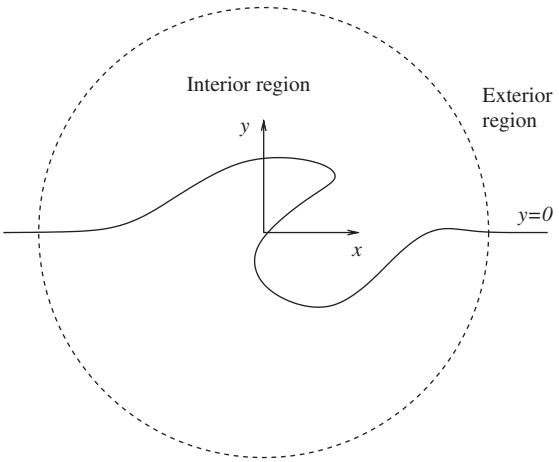

Figure 1. General problem.

For example, the scattering frequency may be high enough that a full method of moments (MoM) scheme [1, 2] to model the whole structure is not feasible, and hence an optics-based method [3] is preferable. However, the embedded feature may be of an electrical size that is best modelled by MoM rather than by using an optics approximation.

Within the literature, this problem is classified into two distinct types: those for which the embedded feature lies above the ground plane and those problems for which it lies below. For the first class, traditional MoM solutions use equivalent currents to represent an equivalent electric current density on the protrusion. Image theory is then used to replace the ground plane with an equivalent imaged current beneath the plane [2]. The second class has been solved by a number of techniques [4–6]. In this case, the ground plane is closed and an equivalent magnetic current represents the tangential electric field in the aperture plane. An exterior problem is solved and an interior problem is also solved to determine the currents on the perfectly electric conducting (PEC) perturbation and in the aperture. However, the general case (Figure 1) does not readily fall into either category, and it is unclear whether a solution can be obtained by using existing methods. In preference, a different approach is desired which models, rather than removes, the infinite ground plane. In particular, methods can be adapted from finite element analysis, in which the far-field domain is modelled by infinite elements for wave-type problems [7]. Applications to electromagnetic wave scattering have been developed by using *hp*-adaptive finite elements, some of which include the use of infinite elements and ground planes [8–10]. Furthermore, infinite boundary elements have been used for static problems [11] and also for wave-type problems [12]. However, this approach [12] uses computationally intensive high Gaussian point integration schemes in the far field.

In the present paper, the infinite boundary element formulation is extended for electromagnetic problems and an accurate low point integration scheme is introduced. This has the advantage that a formulation for problems in which the embedded feature lies both above and below the ground plane (Figure 1) can be readily obtained. This set of problems encompasses the class of problems where the embedded feature lies above the ground plane and also the class of problems where it lies below. In order to test the accuracy of the formulation, we choose a test problem

DOI: 10.1002/nme

for which there is a known analytic solution; the formulation is tested for the specific problem of two-dimensional (2D) transverse magnetic (TM) mode electric field integral equation (EFIE) boundary element formulation of the time harmonic Maxwell equations for incident plane waves; in particular, consider the problem of scattering from a PEC semi-circular cylindrical protrusion whose axis lies along an infinite PEC ground plane. This problem has an analytic solution in the form of a Bessel function expansion and hence can be used to test the accuracy of the new approach. The formulation shall be presented together with results from the test problem. The RCS results will be presented for $ka=1$, where k is the wave number and a is the semi-circular radius for various angles of incidence of the incoming plane wave, and compared with the analytic solution given in the form of a Bessel function expansion.

2. THE FIELD EQUATIONS

In this section, the 2D frequency domain EFIE integral representation is obtained from Maxwell's 3D electromagnetic field equations. This follows closely the derivation of integral formulations given in Wang [1] and Moore and Pizer [2].

First, a time harmonic variation $e^{j\omega t}$ is assumed, where j is the imaginary number $j^2=-1$ and t is the time. This leads to the frequency domain formulation of Maxwell's equations. Then, the median is assumed to be homogeneous with permittivity ε and permeability μ, and the current is assumed to be ohmic conduction. This leads to the existence of two potentials, the vector potential $\mathbf{A}$ and the scalar potential ϕ which satisfy the Helmholtz equation and thus can be represented by surface integrals. The boundary condition for a PEC surface is then applied to enable a closed self-consistent formulation. This formulation is then considered in 2D for the perturbation vector potential $\mathbf{A}^{\mathrm{p}}$ and the perturbation scalar potential ϕ^{p}. Using the perturbation potentials has the advantage that far from the embedded topological feature, in the far field, the form of decay of the perturbation potentials is known from applying Sommerfeld's radiation condition.

2.1. Maxwell's 3D electromagnetic field equations

The starting point is Maxwell's equations in the time domain [1]:

$$\begin{aligned} \nabla\wedge\mathbf{E}(\mathbf{x},t) &= -\frac{\partial}{\partial t}\mathbf{B}(\mathbf{x},t) \\ \nabla\cdot\mathbf{D}(\mathbf{x},t) &= \rho(\mathbf{x},t) \\ \nabla\wedge\mathbf{H}(\mathbf{x},t) &= \frac{\partial}{\partial t}\mathbf{D}(\mathbf{x},t)+\mathbf{J}(\mathbf{x},t) \\ \nabla\cdot\mathbf{B}(\mathbf{x},t) &= 0 \end{aligned} \tag{1}$$

where

$$\begin{aligned} \mathbf{E}(\mathbf{x},t) &= \text{electric field intensity vector} \\ \mathbf{D}(\mathbf{x},t) &= \text{electric displacement vector} \\ \mathbf{H}(\mathbf{x},t) &= \text{magnetic field intensity vector} \end{aligned}$$

DOI: 10.1002/nme

$$\begin{aligned}\mathbf{B}(\mathbf{x},t) &= \text{magnetic induction vector}\\ \mathbf{J}(\mathbf{x},t) &= \text{current density vector}\\ \rho(\mathbf{x},t) &= \text{volume density of electric current}\end{aligned} \tag{2}$$

such that $\mathbf{x}$ is the vector position (x, y, z) in 3D Cartesian coordinates, $\wedge$ is the cross-product and ∇ is the vector differential operator $(\partial/\partial x, \partial/\partial y, \partial/\partial z)$ in Cartesian coordinates.

2.2. Frequency-domain version of Maxwell's equations

By assuming a time variation proportional to $e^{j\omega t}$, the real quantities in the time-domain Maxwell equations can be replaced by complex quantities in the frequency-domain version such that

$$\begin{aligned}\nabla\wedge\mathbf{E}(\mathbf{x}) &= -j\omega\mathbf{B}(\mathbf{x})\\ \nabla\cdot\mathbf{D}(\mathbf{x}) &= \rho(\mathbf{x})\\ \nabla\wedge\mathbf{H}(\mathbf{x}) &= j\omega\mathbf{D}(\mathbf{x})+\mathbf{J}(\mathbf{x})\\ \nabla\cdot\mathbf{B}(\mathbf{x}) &= 0\end{aligned} \tag{3}$$

2.3. Homogeneous materials assumption

For homogenous materials, $\mathbf{D}=\varepsilon\mathbf{E}$ and $\mathbf{B}=\mu\mathbf{H}$, where ε and μ are the permittivity and permeability, respectively, and independent of position. The equation set (3) then reduces to

$$\begin{aligned}\nabla\wedge\mathbf{E}(\mathbf{x}) &= -j\omega\mu\mathbf{H}(\mathbf{x})\\ \nabla\cdot\mathbf{E}(\mathbf{x}) &= \rho(\mathbf{x})/\varepsilon\\ \nabla\wedge\mathbf{H}(\mathbf{x}) &= j\omega\varepsilon\mathbf{E}(\mathbf{x})+\mathbf{J}(\mathbf{x})\\ \nabla\cdot\mathbf{H}(\mathbf{x}) &= 0\end{aligned} \tag{4}$$

Furthermore, $\mathbf{J}$ is assumed to be an ohmic conduction current such that

$$\mathbf{J}=\sigma\mathbf{E} \tag{5}$$

where σ is the conductivity of the medium.

2.4. Integral representation by the vector and scalar potentials

The equation set (4) leads to the identity

$$\mathbf{E}=-j\omega\mathbf{A}-\nabla\phi \tag{6}$$

for the vector potential $\mathbf{A}$ and scalar potential ϕ given by

$$\nabla^2\mathbf{A}+k^2\mathbf{A}=-\mu\mathbf{J} \tag{7}$$

and

$$\nabla^2\phi+k^2\phi=-\rho/\varepsilon \tag{8}$$

DOI: 10.1002/nme

where ∇^2 is the Laplacian operator $\partial^2/\partial x^2, \partial^2/\partial y^2, \partial^2/\partial z^2$ in the Cartesian coordinates, and $k^2=\omega^2\varepsilon\mu$. The Lorentz condition $\nabla\cdot\mathbf{A}=-\mathrm{j}\omega\varepsilon\mu\phi$ has also been imposed on ϕ. The boundary condition between two different materials for the EFIE formulation is

$$\mathbf{E}\wedge\mathbf{n}=(0,0,0) \tag{9}$$

which completes the EFIE formulation.

2.5. 2D representation for the vector and scalar perturbed potentials

In the 2D formulation, the Helmholtz equation is still satisfied for the vector potential (7) and the scalar potential (8). For PEC surfaces, the current and charge lie on the surface. Hence, the vector and scalar potentials satisfy the Helmholtz equation except on the surface. This means that they can be represented by a distribution of Green's functions for the 2D Helmholtz equation over the surface. The strength of Green's function can be determined from (7) for the vector potential and from (8) for the scalar potential, and this is given in [1, 2]. Hence, the vector and scalar potentials can be represented by the integral form

$$\mathbf{A}(\mathbf{x})=\mu\int_C \mathbf{J}(\mathbf{x}')G(|\mathbf{x}-\mathbf{x}'|)\,\mathrm{d}l' \tag{10}$$

and

$$\phi(\mathbf{x})=-\frac{1}{\mathrm{j}\omega\varepsilon}\int_C \nabla'\cdot\mathbf{J}(\mathbf{x}')G(|\mathbf{x}-\mathbf{x}'|)\,\mathrm{d}l' \tag{11}$$

where $G(\mathbf{x})$ is Green's function $G(\mathbf{x})=H_0(kr)/(4\mathrm{j})$, H_0 is the Hankel source function [13, Chapter 9]; C is the PEC surface contour that stretches along the ground plane which is infinite in extent including topological feature which is embedded within the ground plane; the prime superscript denotes variables evaluated on this contour such that the element of length on the contour is $\mathrm{d}l'$ and $\mathbf{x}'$ is a point on the contour; and the 2D radius is $r=\sqrt{x^2+y^2}$. In 2D flow, there is no dependence on the coordinate $\mathbf{z}$, and hence the position vector $\mathbf{x}$ is now given by (x, y) in 2D Cartesian coordinates.

The boundary condition (9) reduces to

$$\begin{aligned}\mathbf{E}_{\tan}&=\mathbf{E}^{\mathrm{i}}_{\tan}+\mathbf{E}^{\mathrm{s}}_{\tan}=0\\ \mathbf{E}^{\mathrm{i}}_{\tan}&=\mathrm{j}\omega\mathbf{A}_{\tan}+\nabla\phi_{\tan}\end{aligned} \tag{12}$$

where the subscript tan refers to the tangent of the vector, the superscript i refers to the incident electric field, the superscript s refers to the scattered electric field, and $\mathbf{A}$ and ϕ are the potentials of the scattered electric field.

Assuming a TM uniform incident field subtended by an angle $-\alpha$, then

$$\begin{aligned}\mathbf{E}^{\mathrm{i}}&=E\mathrm{e}^{-\mathrm{j}ks^{\mathrm{i}}}\hat{\mathbf{e}}^{\mathrm{i}}\\ s^{\mathrm{i}}&=x\cos\alpha-y\sin\alpha,\quad \hat{\mathbf{e}}^{\mathrm{i}}=(\sin\alpha,\cos\alpha)\end{aligned} \tag{13}$$

DOI: 10.1002/nme

In the absence of any embedded topological feature in the flat ground plane, a scattered field is expected, given by the reflected E-field of geometrical optics such that the angle of incidence is the angle of refection; hence,

$$\begin{aligned} \mathbf{E}^{\mathrm{r}} &= E\mathrm{e}^{-\mathrm{j}ks^{\mathrm{r}}}\hat{\mathbf{e}}^{\mathrm{r}} \\ s^{\mathrm{r}} &= x\cos\alpha + y\sin\alpha, \quad \hat{\mathbf{e}}^{\mathrm{r}} = (-\sin\alpha, \cos\alpha) \end{aligned} \tag{14}$$

assuming a ground plane along $y=0$. The inclusion of an embedded topological feature gives a perturbation $\mathbf{E}^{\mathrm{p}}$ to this scattered field, such that

$$\mathbf{E}^{\mathrm{s}} = \mathbf{E}^{\mathrm{r}} + \mathbf{E}^{\mathrm{p}} \tag{15}$$

So far from the embedded feature we expect $\mathbf{E}^{\mathrm{p}}$ to decay to zero.

The boundary condition can then be expressed as

$$\mathbf{E}^{\mathrm{i}}_{\mathrm{tan}} - \mathbf{E}^{\mathrm{r}}_{\mathrm{tan}} = \mathrm{j}\omega\mathbf{A}^{\mathrm{p}}_{\mathrm{tan}} + \nabla\phi^{\mathrm{p}}_{\mathrm{tan}} \tag{16}$$

where $\mathbf{A}^{\mathrm{p}}$ and ϕ^{p} are the perturbed vector and scalar potentials, given by

$$\begin{aligned} \mathbf{A}^{\mathrm{p}}(\mathbf{x}) &= \mu\int_C \mathbf{J}^{\mathrm{p}}(\mathbf{x}')G(|\mathbf{x}-\mathbf{x}'|)\,\mathrm{d}l' \\ \phi^{\mathrm{p}}(\mathbf{x}) &= -\frac{1}{\mathrm{j}\omega\varepsilon}\int_C \nabla'.\mathbf{J}^{\mathrm{p}}(\mathbf{x}')G(|\mathbf{x}-\mathbf{x}'|)\,\mathrm{d}l' \end{aligned} \tag{17}$$

such that $\mathbf{J}^{\mathrm{p}}$ is the perturbed surface current density. The decay of the perturbed variables is discussed next, together with the MoM discretization scheme for (17).

2.6. The numerical method

Combining (16) and (17) gives an equation for the unknown surface current $\mathbf{J}^{\mathrm{p}}$ which can be solved numerically. The starting point for the numerical scheme is the discretization of combined equations (16) and (17) in order to determine the surface current. Once this is found, then (17) can be used to determine the potentials $\mathbf{A}^{\mathrm{p}}$ and ϕ^{p} at any point in the field; hence from (6) we can find the electric field $\mathbf{E}$ at any point. We now consider the shape and weighting functions for the surface current $\mathbf{J}^{\mathrm{p}}$ in both near and far fields.

3. SHAPE AND WEIGHTING FUNCTIONS

The domain is divided into two regions, a near-field region and a far-field region. The embedded feature is contained in the near-field region, and the standard linear shape and weighting functions are used to model the vector and scalar potentials. The far-field region is assumed to be sufficiently far from the embedded feature so that the perturbed potentials and perturbed current are modelled by functions that decay to zero. The particular order of decay is determined from Sommerfeld's radiation condition. As the wave number k increases, the variables only begin to start decaying further away from the body. Hence, the boundary between the near and far fields is dependent upon the wave number. In this paper, the problem considered is a semi-circular protrusion of radius $a=1$ lying above an infinite flat ground plane such that $ka=1$. In this particular case, the boundary

DOI: 10.1002/nme

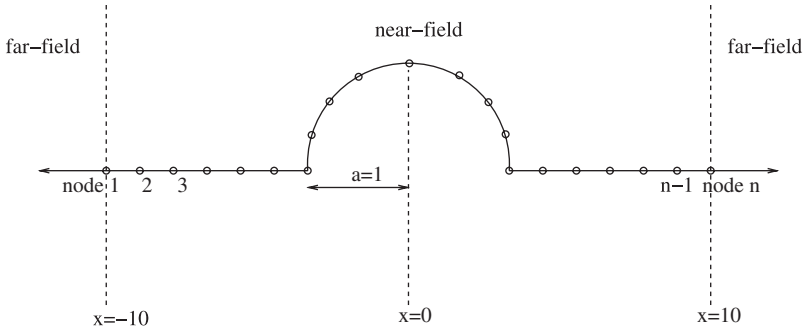

Figure 2. The discretization of the contour.

between the near and far fields given by a distance $x=10$ from the protrusion was found to be sufficient.

Consider discretizing the surface contour of the ground plane and evaluating the variables in the weak formulation of the MoM discretization at n points. Let the points labelled $i=1$ and n lie on the far-field boundary and the points labelled $2\leqslant i\leqslant n-1$ lie in the near field, see Figure 2.

Then (17) becomes

$$\begin{aligned}\int_C \mathbf{W}_q.\mathbf{A}^{\mathrm{p}}(\mathbf{x})\,\mathrm{d}l &= \mathrm{j}\omega\int_C \mathbf{W}_q.\mu\left\{\int_C \sum_{i=1}^{n}\mathbf{N}_i(\mathbf{x}')J_i G(|\mathbf{x}-\mathbf{x}'|)\,\mathrm{d}l'\right\}\mathrm{d}l\\ \int_C \mathbf{W}_q\cdot\nabla\phi^{\mathrm{p}}(\mathbf{x})\,\mathrm{d}l &= \int_C(\mathbf{W}_q\cdot\nabla)\left\{-\frac{1}{\mathrm{j}\omega\varepsilon}\int_C\sum_{i=1}^{n}\nabla'\cdot\mathbf{N}_i(\mathbf{x}')J_i G(|\mathbf{x}-\mathbf{x}'|)\,\mathrm{d}l'\right\}\mathrm{d}l\end{aligned} \tag{18}$$

where n weighting functions, $1\leqslant q\leqslant n$, denoted by $\mathbf{W}_q$ are considered, and the surface current vector is discretized by

$$\mathbf{J}^{\mathrm{p}}=\sum_{i=1}^{n}\mathbf{N}_i J_i \tag{19}$$

where J_i is the current density at node i, and $\mathbf{N}_i$ is the vector shape function for node i.

In the MoM formulation, the physical variables are evaluated at each node point only. The particular weighting and shape functions chosen in the near and far fields are now discussed.

3.1. Shape functions in the near field

The elements denoted by the subscript i such that $2\leqslant i\leqslant n-1$ lie wholly in the near field and standard linear element shape functions are used. This means that in the near field region, at least 10 nodes per wavelength are required to model the oscillatory variation of the surface current. Hence, standard rather than special elements are used in the near-field region. The special oscillatory decay elements are used only in the far field. The standard linear 2D shape function is described pictorially in Figure 3 and is made up of two linear segments, N_{i_-} preceding node i and N_{i_+} after node i, and the two segments join at the central node i.

DOI: 10.1002/nme

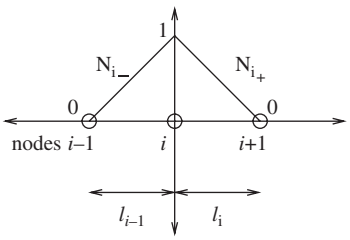

Figure 3. The shape function for element i.

This element encompasses three nodes and two linear segments such that

$$\mathbf{N}_i = \mathbf{N}_{i_-} = N_{i_-}\hat{\mathbf{l}}_{i-1} \quad \text{for node } i-1 \text{ to } i,\ N_{i_-} = 1 + l/l_{i-1}$$

$$\mathbf{N}_i = \mathbf{N}_{i_+} = N_{i_+}\hat{\mathbf{l}}_i \quad \text{for node } i \text{ to } i+1,\ N_{i_+} = 1 - l/l_i$$

where l_i is the distance between nodes i and $i+1$; $\hat{\mathbf{l}}_i$ is the vector direction of the straight line between nodes i and $i+1$; and l is the distance measure from node i along the contour C. When $l=0$, $N_{i_-} = N_{i_+} = 1$ is the value at node i. When $l = -l_{i-1}$, $N_{i_-} = 0$ is the value at node $i-1$. When $l = l_{i+1}$, $N_{i_+} = 0$ is the value at node $i+1$.

3.2. Shape functions in the far field

The advantage of using the perturbed variables is that they must decay to zero in the far field, and this decay rate can be determined from Sommerfield's radiation condition [14]. Let us assume that in the far field the perturbed current density has the form of a radiated wave given by

$$\mathbf{J}^{\mathrm{p}} = \mathrm{const} * \mathrm{e}^{-\mathrm{j}kr}/\sqrt{r} \tag{20}$$

where const is a complex constant. It is seen that (20) satisfies the Sommerfield radiation condition [14].

There are two elements that have part of their domain in the far field. These are elements positioned at nodes $i=1$ and n. For node $i=1$: $\mathbf{N}_1 = \mathbf{N}_{1_-} = N_{1_-}\hat{\mathbf{x}}$ from $x=-\infty$ to node 1; $\mathbf{N}_1 = \mathbf{N}_{1_+} = N_{1_+}\hat{\mathbf{l}}_1$ from node 1 to node 2; hence, the element stretches to infinite extent $x=-\infty$. The far-field variation (20) is modelled by the oscillatory decay function

$$N_{1_-} = \sqrt{\frac{|x_1|}{|x|}}\mathrm{e}^{-\mathrm{j}k(|x|-|x_1|)} \tag{21}$$

where (x_i, y_i) is the co-ordinate position of node i. Furthermore, $N_{1_-} = 1$ at $x = x_1$ and $N_{1_-} = 0$ at $x = -\infty$. This is described pictorially in Figure 4.

Similarly, for node $i=n$: $\mathbf{N}_n = \mathbf{N}_{n_-} = N_{n_-}\hat{\mathbf{l}}_{n-1}$ from node $n-1$ to node n; $\mathbf{N}_n = \mathbf{N}_{n_+} = N_{n_+}\hat{\mathbf{x}}$ from node n to $x=\infty$ where

$$N_{n_+} = \sqrt{\frac{x_n}{x}}\mathrm{e}^{-\mathrm{j}k(x-x_n)} \tag{22}$$

DOI: 10.1002/nme

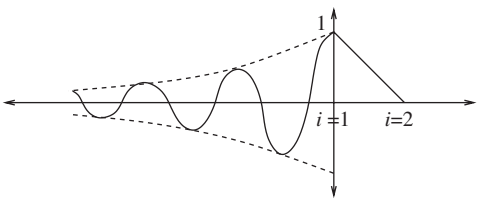

Figure 4. Real part of the shape function at node 1.

3.3. Weighting functions

In the near field, the weighting functions for elements $2 \leqslant i \leqslant n-1$ are chosen to be the same as the shape functions; hence, $\mathbf{W}_i = \mathbf{N}_i$. For elements positioned at $i=1$ and n, which have part of their domain in the far field, the following variation is chosen:

For node $i=1$: $\mathbf{W}_1 = \mathbf{W}_{1\_} = W_{1\_}\hat{\mathbf{x}}$ from node 0 to node 1, $W_{1\_} = 1 + l/l_0$; $\mathbf{W}_1 = \mathbf{W}_{1_+} = N_{1_+}\hat{\mathbf{l}}_1$ from node 1 to node 2, where node 0 is defined as being in position $(x_1 - l_0, 0)$ and $l_0 = l_1$.

For node $i=n$: $\mathbf{W}_n = \mathbf{W}_{n\_} = N_{n\_}\hat{\mathbf{l}}_n$ from node $n-1$ to node n, $\mathbf{W}_n = \mathbf{W}_{n_+} = W_{n_+}\hat{\mathbf{x}}$ for node n to node $n+1$, $W_{n_+} = 1 - l/l_{n+1}$ where node $n+1$ is defined as being in position $(x_n + l_{n+1}, 0)$ and $l_{n+1} = l_n$.

Hence, all the weighting functions are standard linear basis functions. (Since an element for the weighting functions stretches over three nodes (see Figure 3), the central point of the element is taken to be at a nodal point.) However, we shall consider the weak form of the integral by using Stokes' identity in order to reduce the number of differentials acting upon the surface current by 1 and thus improve the accuracy of the formulation. Because of this, the linear basis function representation must be used as the differential operator acting on the delta function basis of point collocation is undefined. Hence, once the weak form is used then we must adopt the one-point Gauss procedure used in the paper rather than point collocation.

4. MATRIX FORMULATION

Substituting the shape function expansion for the current into the integral equation expressions for the vector potential and scalar potential functions and integrating the expressions over the whole space with each of the weighting functions gives

$$A_{qi} = \mathrm{j}\omega \int_q \mathbf{W}_q \cdot \left\{ \mu \int_i \mathbf{N}_i(\mathbf{x}') G(|\mathbf{x} - \mathbf{x}'|)\, \mathrm{d}l' \right\} \mathrm{d}l \tag{23}$$

$$\phi_{qi} = -\int_q \nabla \cdot \mathbf{W}_q \left\{ -\frac{1}{\mathrm{j}\omega\varepsilon} \int_i \nabla' \cdot \mathbf{N}_i(\mathbf{x}') G(|\mathbf{x} - \mathbf{x}'|)\, \mathrm{d}l' \right\} \mathrm{d}l, \quad 1 \leqslant i, \ q \leqslant n \tag{24}$$

since Stoke's identity $\int_c \mathbf{W}_q \cdot \nabla\phi \, \mathrm{d}l = -\int_c \nabla \cdot \mathbf{W}_q \phi \, \mathrm{d}l$ holds for this particular choice of weighting functions. The integral $\int_q$ denotes the integral over the weighting function element q, and the integral $\int_i$ denotes the integral over the shape function element i. Thus, all the integrals are finite

DOI: 10.1002/nme

in length except the integrals over shape function elements $i=1$ and n which are infinite in length. The boundary condition contribution is given by

$$e_q = \int_q \mathbf{W}_q.(\mathbf{E}^{\mathrm{i}} - \mathbf{E}^{\mathrm{r}})\,\mathrm{d}l \tag{25}$$

The matrix equation is

$$Z_{qi}\,J_i = e_q \tag{26}$$

where

$$Z_{qi} = A_{qi} + \phi_{qi}$$

and $1 \leqslant q, i, \leqslant n$.

The outer integral is calculated using 1-point Gauss. The matrix terms A_{qi} and ϕ_{qi} then reduce to

$$\begin{aligned} A_{qi} = \frac{\omega\mu}{16}[&2l_{q-1}(a_{q-i-}\cos(\theta_{q-1}-\theta_{i-1}) \\ &+a_{q-i+}\cos(\theta_{q-1}-\theta_i)) \\ &+2l_q(a_{q+i-}\cos(\theta_q-\theta_{i-1}) \\ &+a_{q+i+}\cos(\theta_q-\theta_i))] \end{aligned}$$

where

$$a_{q-i-} = \int_{l_{i-1}}^{l_i} N_{i-}(\mathbf{x}')H_0(k(\mathbf{x}'-\mathbf{x}_q^{\mathrm{c}}))\,\mathrm{d}l' \tag{27}$$

and similarly for a_{q-i+}, a_{q+i-} and a_{q+i+}; $\mathbf{x}_q^{\mathrm{c}}$ is the position of the centre point between nodes q and $q+1$; θ_i is the angle measure in the range $0 \leqslant \theta \leqslant 2\pi$ subtended by the straight line from the point i to the point $i+1$ and the x-axis.

Similarly,

$$\phi_{qi} = -\frac{1}{8\omega\varepsilon}(\phi_{q-i-} - \phi_{q-i+} - \phi_{q+i-} + \phi_{q+i+}) \tag{28}$$

where

$$\phi_{q-i-} = \frac{1}{l_{i-1}}\int_{l_{i-1}}^{l_i} H_0(k(\mathbf{x}'-\mathbf{x}_q^{\mathrm{c}}))\,\mathrm{d}l' \tag{29}$$

and similarly for ϕ_{q-i+}, ϕ_{q+i-} and ϕ_{q+i+}.

The standard approach is used for contributions from finite boundary elements and the inner integrals are calculated using 2-point Gauss. For infinite boundary elements, the contributions

DOI: 10.1002/nme

involve infinite integral evaluations. For example, the contribution from the term $a_{1\_1\_}$ is

$$\begin{aligned} a_{1\_1\_} = {} & 2\sqrt{|x_1|}\mathrm{e}^{\mathrm{j}k|x_1|} \\ & \times \left\{ \int_{|x_1|}^{|x_0|} \frac{\mathrm{e}^{-\mathrm{j}kx'}}{\sqrt{x'}} [H_0(kr_0'^{\mathrm{c}}) - \sin g(kr_0'^{\mathrm{c}})]\,\mathrm{d}x' \right. \\ & + \int_{|x_1|}^{|x_0|} \frac{\mathrm{e}^{-\mathrm{j}kx'}}{\sqrt{x'}} \sin g(kr_0'^{\mathrm{c}})\,\mathrm{d}x' \\ & \left. + \int_{|x_0|}^{|x_\infty|} \frac{\mathrm{e}^{-\mathrm{j}kx'}}{\sqrt{x'}} H_0(kr_0'^{\mathrm{c}})\,\mathrm{d}x' \right\} \end{aligned}$$

where $\sin g(kr) = 1 - (2\mathrm{j}/\pi)\log(\gamma kr/2)$ and r_q^{c} is the distance measured from the centre point of the element q, and γ is Euler's constant. There are similar contributions from the scalar potential ϕ.

5. INFINITE BOUNDARY ELEMENT INTEGRATIONS

Most of the integral contributions represented by (23) and (24) are finite. However, the integrals will be infinite in extent for $i = 1$ and n. In particular, the integrands in these integral expressions for $\phi_{q\_1\_}$, $\phi_{q+1\_}$, $a_{q\_1\_}$, $a_{q+1\_}$, ϕ_{q_n+}, ϕ_{q+n+}, a_{q_n+} and a_{q+n+} are oscillatory and infinite in extent. Special integration rules are required and introduced. All these integrals have the form

$$I = \int_{p_1}^{\infty} h(x; b)\,\mathrm{d}x \tag{30}$$

where $h(x; b)$ is singular at the point $x = b < p_1$. For the test example used here, the border between the near and far fields is positioned at $x = 10$; hence $p_1 = 10$. Near to this singularity, the behaviour is of the order $H_0(k(x-b)) \sim \log(x-b)$ and in the field far from the singularity, the integrand is $h(x; b) \sim \mathrm{e}^{-2\mathrm{j}kx}/x$.

To calculate (30), this far-field integral is therefore divided into a near-singularity integral and a far-singularity integral so that the singularity behaviour in the respective regions can be closely approximated.

Since the far field starts at a distance p_1 from the embedded feature it is assumed that the far-singularity integrand approximation, which is that $h(x; b) \sim \mathrm{e}^{-2\mathrm{j}kx}/x$, holds at a distance p_1 from the singularity at $x = b < p_1$. This will always be satisfied if $x > 2p_1$, because the distance from the singularity is greater than p_1, the far-field distance. This condition is used to provide an upper limit for the near-singularity integral interval.

The near-singularity integral interval is split into several sub-intervals in such a way that both the execution time and the inaccuracy of the numerical calculation are kept at a minimum. Hence, there is a trade-off between execution time and accuracy, as represented in Figure 5.

To reduce the execution time for the integral evaluation, each interval increases in size away from the point p_1. Hence, the proportion increase, denoted by the ratio r, is greater than the

DOI: 10.1002/nme

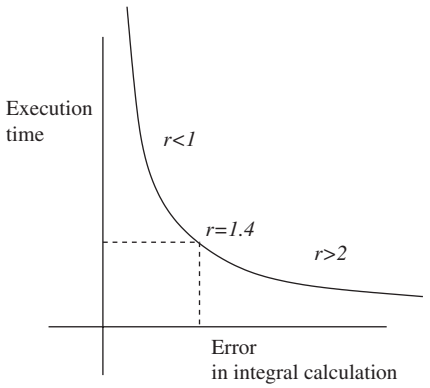

Figure 5. Execution time *versus* accuracy.

value 1. However, if the value 2 is chosen, simple tests show noticeable inaccuracies for typical integral evaluations.

To reduce the inaccuracy of the numerical calculation, it was decided to choose the value 1.4 (see Figure 5). This factor appears to be independent of the wave number, which determines the rapidity of the oscillations, but dependent upon the decay of the envelope of the wave oscillations. Finally, each integral evaluation is approximated by assuming that the envelope of the integrand varies as a quadratic polynomial.

To recap, the near-singularity integral is evaluated by dividing it into $m+2$ integrals, which are calculated independently, and by finding the smallest m such that the inequality $b+\delta(1.4)^{m+1} > 2p_1$ holds, where $\delta = b - p_1$. The $m+2$ integrals are

$$I = \left(\sum_{i=0}^{m} \int_{x=b+\delta(1.4)^i}^{x=b+\delta(1.4)^{i+1}} h(x;b)\,\mathrm{d}x \right) + \int_{x=b+\delta(1.4)^{m+1}}^{\infty} h(x;b)\,\mathrm{d}x \tag{31}$$

This is described pictorially by Figure 6.

The near-singularity integrals are approximated by

$$\int_{q1}^{q2} h(x;b)\,\mathrm{d}x \sim \int_{q1}^{q2} (a_0 + a_1 x + a_2 x^2) \mathrm{e}^{-2\mathrm{j}kx}\,\mathrm{d}x \tag{32}$$

The integrand is sampled at three points, q_1, q_2 and $q_3 = (q_1+q_2)/2$ in order to determine the constants a_0, a_1 and a_2 of (32).

The far-singularity integral is evaluated by assuming that the integrand has the form $h(x;b) \sim \mathrm{e}^{-2\mathrm{j}kx}/x$; hence it is approximated by

$$\int_{q1}^{\infty} h(x;b)\,\mathrm{d}x \sim \int_{q1}^{\infty} (a_0 + a_1 x + a_2 x^2) \frac{\mathrm{e}^{-2\mathrm{j}kx}}{x^3}\,\mathrm{d}x \tag{33}$$

where the integrand is sampled at three points, $q_1 = 2p_1$, $q_2 = 2q_1$ and $q_3 = (q_1+q_2)/2$ in order to determine the constants a_0, a_1 and a_2 of (33). This integral is expressed in terms of

DOI: 10.1002/nme

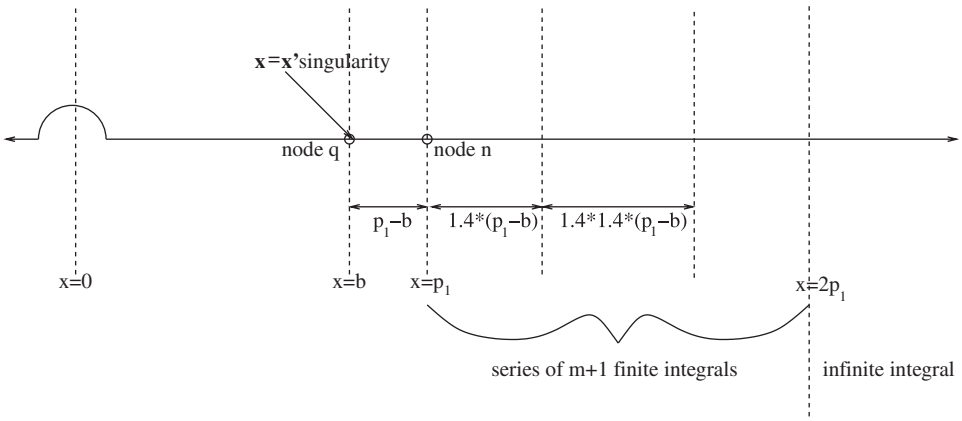

Figure 6. The divisions of the far-field integral.

the integral

$$
\begin{aligned}
I_1 &= \int_{q1}^{\infty} \frac{\mathrm{e}^{-2\mathrm{j}kx}}{x}\,\mathrm{d}x = \int_{2kq_1}^{\infty} \frac{\mathrm{e}^{-\mathrm{j}x}}{x}\,\mathrm{d}x \\
&= \int_{2kq_1}^{\infty} \frac{\cos x}{x}\,\mathrm{d}x - \mathrm{j}\int_{2kq_1}^{\infty} \frac{\sin x}{x}\,\mathrm{d}x \\
&= -C\mathrm{i}(2kq_1) + \mathrm{j}(S\mathrm{i}(2kq_1) - \pi/2)
\end{aligned}
$$

where

$$
\begin{aligned}
C\mathrm{i}(z) &= f(z)\sin z - g(z)\cos z \\
S\mathrm{i}(z) &= \pi/2 - f(z)\cos z - g(z)\sin z
\end{aligned}
$$

Rational approximations for $f(z)$ and $g(z)$ are given in [13, 5.2.38 and 5.2.39, p. 233].

6. RCS CALCULATION

It is assumed that the largest order contribution to the RCS is from near to the embedded feature. Then the scattered far field is given by

$$
\mathbf{E}^{\mathrm{s}}(r,\theta).\hat{\boldsymbol{\phi}} = -\mathrm{j}\omega\mathbf{A}.\hat{\boldsymbol{\phi}} = -\frac{\omega\mu}{4}\int_c \mathbf{J}(l').\hat{\boldsymbol{\phi}} H_0(kr^*)\,\mathrm{d}l' \tag{34}
$$

where $r^* = \sqrt{(r^2 - 2rr'\cos(\theta-\theta') + r'^2)}$.

DOI: 10.1002/nme

Assuming that the greatest contributions to the integral are from values such that $r' \ll r$, then $r^* \sim r - r'\cos(\theta - \theta') + O(1/r)$ and for large r^*

$$H_0(kr^*) \sim \sqrt{\frac{2}{\pi k r^*}} \mathrm{e}^{-\mathrm{j}k(r'-\pi/4)}$$

The scattered far field is then given by

$$\mathrm{e}^{\mathrm{j}kr}\sqrt{(r)}\mathbf{E}^{\mathrm{s}}(r,\phi).\hat{\boldsymbol{\phi}} = \left(\frac{-\omega\mu}{4}\right)\sqrt{\frac{2}{\pi k}}\mathrm{e}^{\mathrm{j}k\pi/4} \times \sum_{i=1}^{n}\int_c \mathbf{N}_i(\mathbf{x}').\hat{\boldsymbol{\phi}}\mathrm{e}^{\mathrm{j}kr'\cos(\phi-\theta')}\,\mathrm{d}l' \tag{35}$$

The linear (as opposed to decibel scale) RCS can then be obtained from the definition

$$\mathrm{RCS} = \lim_{r\to\infty}\left\{2\pi r\frac{|\mathbf{E}^{\mathrm{s}}|^2}{|\mathbf{E}^{\mathrm{i}}|^2}\right\} \tag{36}$$

Integrals are then obtained of the form

$$\sin\theta\int_{|x_1|}^{\infty}\frac{\mathrm{e}^{-\mathrm{j}kx'(1+\cos\theta)}}{\sqrt{x'}}\,\mathrm{d}x' \tag{37}$$

and

$$\sin\theta\int_{x_n}^{\infty}\frac{\mathrm{e}^{-\mathrm{j}kx'(1-\cos\theta)}}{\sqrt{x'}}\,\mathrm{d}x' \tag{38}$$

For values of θ such that the integral is not singular, it is of the form

$$I = \int_a^{\infty}\frac{\mathrm{e}^{-\mathrm{j}bx}}{\sqrt{x}}\,\mathrm{d}x \tag{39}$$

where b is non-zero. This is approximated by the Fresnel integrals

$$C(z) - \mathrm{i}S(z) = \frac{1}{\sqrt{2\pi}}\int_0^{\pi z^2/2}\frac{\mathrm{e}^{-\mathrm{j}q}}{\sqrt{q}}\,\mathrm{d}q \tag{40}$$

Fits to these equations are given in [13, 7.3.9 and 7.3.10].

Exceptions are when the integrals become singular. For these cases, we have integrals of the form

$$I = \theta\int_a^{\infty}\frac{\mathrm{e}^{-\mathrm{j}kx\theta^2/2}}{\sqrt{x}}\,\mathrm{d}x = \mathrm{sign}(\theta)\sqrt{\frac{2}{k}}\int_{ka\theta^2/2}^{\infty}\frac{\mathrm{e}^{-\mathrm{j}x}}{\sqrt{x}}\,\mathrm{d}x \tag{41}$$

which can also be determined by the Fresnel integral fits in Abramowitz and Stegun.

DOI: 10.1002/nme

7. RESULTS

Results for the scattered RCS from the semi-circular cylinder radius $a=1$ and wave number $k=1$ at incident wave angles 0, 45 and 90° are given (Figures 7–9). The scale is linear, as given by (36), and logarithms (decibel scale) are not taken. Four hundred nodes are used, and the boundaries between the boundary element/infinite boundary element regions are positioned at $x=-10$ and 10. These results are denoted in the graph legends by 'Infinite B.E.'. By reflecting below the ground plane, the semi-circular cylinder and the ground plane can be replaced by a circular cylinder, and an analytic expansion, in the form of a Bessel function expansion, can be found for the field variables and is denoted in the graph legends by 'Analytic'.

In all the results, the RCS near grazing is less accurate. This is due to the inaccurate modelling of the sharp corner between the semi-circular cylinder and the ground plane, which should be

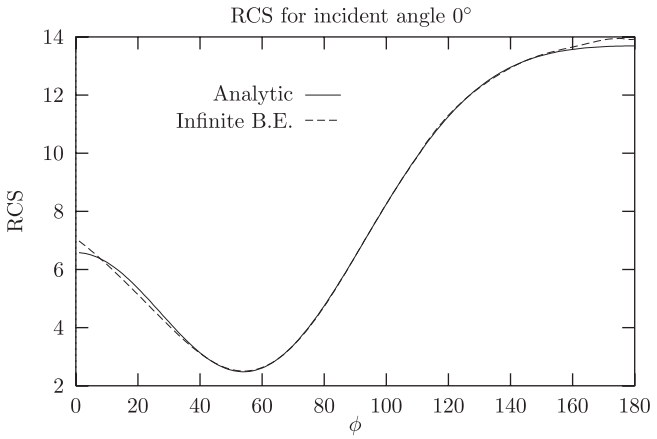

Figure 7. RCS for incident angle 0°.

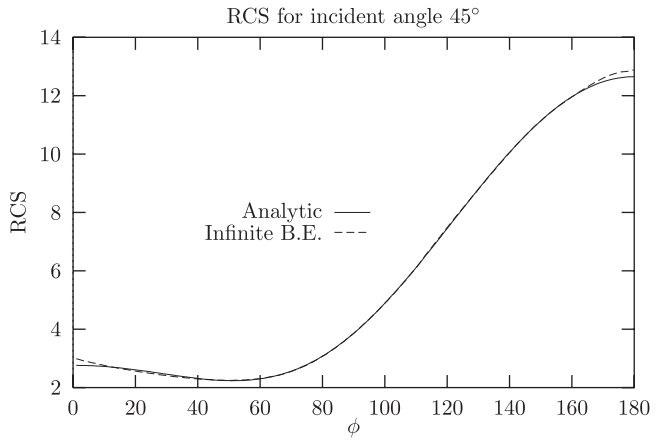

Figure 8. RCS for incident angle 45°.

DOI: 10.1002/nme

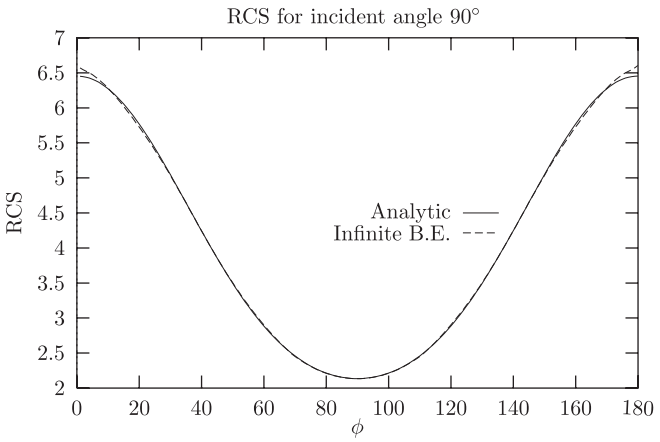

Figure 9. RCS for incident angle 90°.

modelled by a singular shape function of order $1/\sqrt{r}$ for a radial measure r whose co-ordinate origin is at the corner. Future work would be to include the correct singular variation at sharp corners, and it is expected that this inaccuracy will then disappear.

8. CONCLUSION

A MoM formulation for ground plane problems with general types of embedded features, which can lie both above and below the ground plane (see Figure 1), has been presented. Previous research [2, 4–6] has considered the embedded feature lying either wholly above or wholly below the ground plane, and it is unclear whether such methods can be applied for the general case (Figure 1). The accuracy of the formulation was tested against the analytic solution for the specific problem of a semi-circular cylindrical protrusion lying above a flat infinite ground plane. The results give us confidence that the formulation is accurate and will work for the general case in which the feature can lie both partly above and partly below the ground plane, which is a significant advance. Furthermore, it has been shown that low Gaussian point infinite boundary elements can model electromagnetic wave scattering off ground planes. Further developments include using corner elements with appropriate singular behaviour, using higher-order shape functions and analysing the accuracy of the approximation for the current vector in the numerical integration scheme. All these developments should help in reducing the number of nodes used in the mesh.

Future work relates to the development of the method for three-dimensional problems such that the ground plane itself has a weak curvature. To attempt this using standard methods would prove highly complicated if not impossible. The big advantage of the formulation presented here is that, although a weakly curving ground plane was not considered in this paper, it can easily be extended for this case.

This is the first use of infinite boundary elements to model electromagnetic wave scattering problems known to the author, and it is also hoped that the formulation, especially for calculating the far-field element integrals, will be of use in a wide variety of wave-type problems outside of electromagnetics.

DOI: 10.1002/nme

ACKNOWLEDGEMENTS

This work was carried out while the author was employed at BAESYSTEMS, ATC Sowerby, Bristol. The author would like to thank Dr David Rowse and Dr Glenn Gapper of BAESYSTEMS for encouraging and promoting the research.

REFERENCES

1. Wang JJH. *Generalized Moment Methods in Electromagnetics*. Wiley: New York, 1991.
2. Moore J, Pizer R. *Moment Methods in Electromagnetics*. Wiley: New York, 1983.
3. Ruck GT. *Radar Cross-Section Handbook*. Plenum Press: New York, 1970.
4. Harrington RF, Mautz JR. A generalized network formulation for aperture problems. *IEEE Transactions on Antennas and Propagation* 1976; **AP-40**:870–873.
5. Jeng SK. Scattering from a cavity-backed slit in a ground plane—TE case. *IEEE Transactions on Antennas and Propagation* 1990; **AP-38**:1523–1529.
6. Jeng SK, Tzeng ST. Scattering from a cavity-backed slit in a ground plane—TM case. *IEEE Transactions on Antennas and Propagation* 1991; **AP-39**:661–663.
7. Bettess P. *Infinite Elements*. Penshaw Press: Sunderland, U.K., 1992.
8. Ledger PD, Morgan K, Peraire J, Hassan O, Weatherill NP. The development of an *hp*-adaptive finite elements procedure for electromagnetic scattering problems. *Finite Elements in Analysis and Design* 2003; **39**:751–764.
9. Cecot W, Rachowicz W, Demkowicz L. An *hp*-adaptive finite element method for electromagnetics. Part 3: a three-dimensional infinite element for Maxwell's equations. *International Journal for Numerical Methods in Engineering* 2003; **57**:899–921.
10. Rachowicz W, Zdunek A. An *hp*-adaptive finite element method for scattering problems in computational electromagnetics. *International Journal for Numerical Methods in Engineering* 2005; **62**:1226–1249.
11. Beer G, Watson JO. Infinite boundary elements. *International Journal for Numerical Methods in Engineering* 1989; **28**:1233–1247.
12. Bu S. Infinite boundary elements for the dynamic analysis of machine foundations. *International Journal for Numerical Methods in Engineering* 1997; **40**:3901–3917.
13. Abramowitz AM, Stegun IA. *Handbook of Mathematical Functions*. Penshaw Press, Wiley: New York, 1965.
14. Sommerfeld A. Theorie mathematique del la diffraction. *Mathematiische Annalen* 1943; **47**:317–374.

DOI: 10.1002/nme